

A biwavelength analysis of Pioneer Venus polarization observations

Willem Jan J. Knibbe, Johan F. de Haan, and Joop W. Hovenier

Department of Physics and Astronomy, Free University, Amsterdam, The Netherlands

Larry D. Travis

NASA Goddard Institute for Space Studies, New York

Abstract. A new method for analyzing Pioneer Venus polarimetry data on a pixel-wise basis is presented. Quasi-simultaneous observations at two wavelengths (550 and 935 nm) are combined and compared with results of multiple scattering calculations. In this manner, hypotheses about particle size distributions in the upper part of the Venus atmosphere are tested. Particles composed of a sulfuric acid solution are considered, and a distinction is made between large and small particles, called cloud and haze particles, respectively. Three model atmospheres have been investigated: (1) a single layer containing cloud particles, (2) a single layer containing a mixture of cloud and haze particles, and (3) a two layer model with an upper layer composed of haze particles and a lower layer containing cloud particles. It is found that all three models agree with the observations at phase angles near 20° , but that the first model cannot be made to agree with the observations for phase angles near 90° . This confirms the presence of haze particles in the Venus atmosphere found earlier by Kawabata *et al.* [1980]. We find that the haze particles may be situated either above or mixed within the main cloud deck of Venus. We derived effective radii between 0.85 and $1.15\ \mu\text{m}$ for the cloud particles, and effective radii of 0.2 or $0.3\ \mu\text{m}$ for the haze particles. When the haze particles are situated above the cloud layer, the haze optical thickness can take values of up to 0.6 at 550 nm. When the haze particles are mixed with the cloud particles, their contribution to the total atmospheric scattering coefficient at 550 nm can become as large as 70%.

1. Introduction

The thick cloud deck of the planet Venus, as seen from Earth and from satellites, consists mainly of particles composed of a sulfuric acid solution. This article reports on investigations of the sizes of these particles. In order to provide a framework for our investigations, earlier research on Venus' cloud particle sizes is briefly sketched in this section. Here, we use the expression "clouds" loosely to indicate atmospheric regions containing particulate matter.

The first accurate characterization of both composition and sizes of the cloud particles of Venus on a global scale was given by Hansen and Hovenier [1974]. They analyzed earthbound observations of the polarization of Venus. In most of these observations the planetary disk was not resolved and the cloud properties they derived are globally averaged properties.

Hansen and Hovenier [1974] interpreted the polarization of Venus using the simplest relevant cloud model. This model consists of one thick plane parallel layer of spherical particles and includes molecular scattering. The wavelength dependent refractive index of the particles that gave the best fit to the observations corresponds to a concentrated solution of sulfuric acid. The particles are distributed in size according to a fairly narrow gamma distribution, with an effective radius of $1.05\ \mu\text{m}$ and an effective variance of 0.07. These particle characteristics pertain to the upper part of the clouds of Venus, since the polarization of sunlight reflected by a thick cloud layer is mainly due to scattering in the upper part [Hansen and Travis, 1974].

The globally averaged chemical composition of the particles in the upper part of the clouds of Venus, as found by Hansen and Hovenier [1974], is the same as the local chemical composition found by in situ measurements [e.g., Marov *et al.*, 1980; Ragent and Blamont, 1980; Knollenberg and Hunten, 1980; Krasnopol'sky, 1983]. However, it appears that the local particle size distribution in the upper part of the clouds of Venus

is in some, but not all, cases the same as the globally averaged distribution deduced by *Hansen and Hovenier* [1974]. This will be illustrated by the following observations, which all pertain to the upper part of the clouds of Venus.

1. The measurements of nephelometers on board the Venera 9 and 10 entry probes made in 1975 and on board of the Venera 11 entry probe in 1978, as analyzed by *Marov et al.* [1980], indicated a size distribution similar to that found by *Hansen and Hovenier* [1974]. More specifically, a gamma distribution with an effective radius between $1.0\ \mu\text{m}$ and $1.35\ \mu\text{m}$ and an effective variance between 0.04 and 0.09 was found to give good agreement with the experimental data. The effective radius increased when descending deeper in the clouds.

2. Spectroscopic observations of the sunlit limb of Venus performed by the Venera 9 and 10 orbiters [*Krasnopol'sky*, 1983] indicated the presence of particles in the upper part of the clouds of Venus that were smaller than those deduced by *Hansen and Hovenier* [1974]. The effective particle radii of these small particles were found to lie between 0.12 and $0.29\ \mu\text{m}$, increasing with decreasing altitude. These observations pertain to higher altitudes than those analyzed by *Marov et al.* [1980].

3. The measurements performed by the Pioneer Venus sounder probe in 1978 [*Knollenberg and Huntén*, 1980] covered roughly the same altitude range as the Venera measurements analyzed by *Marov et al.* [1980]. However, in addition to one mode of the size distribution similar to the unimodal distribution described by *Hansen and Hovenier* [1974] and by *Marov et al.* [1980], the analysis of *Knollenberg and Huntén* also indicated other modes, one of which was found in the upper part of the clouds of Venus and consists of smaller particles. These smaller particles have radii of the order of $0.18\ \mu\text{m}$. So these measurements indicated a bimodal size distribution of the particles in the upper part of the clouds of Venus.

4. Recent spectral observations of the night side of Venus performed by the spacecraft Galileo, as analyzed by *Grinspoon et al.* [1993], indicated the presence of particles with an average radius of $1.0\ \mu\text{m}$ as well as smaller particles with an average radius of $0.3\ \mu\text{m}$ in the upper part of the clouds of Venus. They inferred that the smaller particles contributed about 15% to the extinction at near-infrared wavelengths.

Though the above-mentioned Venera, Pioneer Venus, and Galileo measurements had a higher spatial resolution than earthbound polarimetry, they could only provide snapshots of the cloud properties of Venus, whereas earthbound polarimetry data cover a large time span. The Pioneer Venus orbiter cloud photopolarimeter (OCP) data, however, combine a higher spatial resolution than earthbound polarimetry with a time coverage running from 1978 till 1990. A first analysis of these data by *Kawabata et al.* [1980] showed that a model containing spherical sulfuric acid particles agreed

with the observations. Averaging the observations over the entire disk and specific regions of the planet, *Kawabata et al.* [1980] found that a thin haze layer of small sulfuric acid particles was present on top of and partly mixed within a cloud layer having similar properties, as found by *Hansen and Hovenier* [1974]. This research has been continued by *Sato et al.* [1996], whose analysis is focused on the long-term behavior of the haze in the polar regions where it is most prominent.

In this paper we consider the evidence, as contained in the Pioneer Venus polarimetry data, on the occurrence of small sulfuric acid particles in the upper Venus atmosphere. For that purpose, we developed a biwavelength analysis which has the advantage that we do not need to average over regions of the planet but may analyze the data on a pixel-wise basis. As a result, information on haze particles is derived from the spectral signature of the polarized light and not from its angular signature. This biwavelength analysis is more accurate than conventional methods that focus on the angular variation of the polarized light because disturbing effects introduced by horizontal variations in the Venus atmosphere are (implicitly) eliminated.

2. Pioneer Venus Orbiter Polarization Observations

The Pioneer Venus orbiter was launched in 1978 and on arrival at Venus in December 1978 was inserted into a highly elliptical nearly polar orbit. For more details concerning the Pioneer Venus orbiter, see *Colin and Huntén* [1977] and *Colin* [1980]. The cloud photopolarimeter has measured the intensity and the degree as well as the direction of the linear polarization in wavelength bands centered at 270, 365, 550, and 935 nm, from distances to the planetary surface between 22,000 and 67,000 km. For details concerning the polarimeter, see *Russell et al.* [1977], *Colin and Huntén* [1977], and *Travis* [1979]. Full-disk observations were obtained in a few hours, employing the spin-scan technique. These measurements were reduced to tables, containing values of the intensity I , degree of linear polarization P , and orientation angle of the polarization χ , at four wavelengths and for each pixel of the sunlit and visible part of Venus. Following the terminology of *Kawabata et al.* [1980], we will refer to these tables as maps. The pixels of these maps correspond to dimensions on the planet of the order of 500 km.

About 2000 maps of the planet were acquired from 1978 to 1990, providing a number of periods of the order of several months for which there was essentially daily coverage. These maps have been cataloged at the Goddard Institute for Space Studies in New York, and form the OCPP database. Below we present detailed results of the analysis of observations at 550 nm and 935 nm of four maps taken at the beginning of the Pioneer Venus mission. Table 1 gives information taken from the OCPP catalog about these maps. Many examples of these data are given by *Kawabata et al.* [1980].

Table 1. Catalog Data of the OCPP Maps Analyzed in This Paper

Map	Orbit	Date	Time, UT	α_0	Altitude, km	β_{orb}	λ_{orb}	β_{sun}	λ_{sun}
16	9	Dec. 13, 1978	0236:43	97.1	32936.4	13.5	19.1	-1.5	-77.9
21	10	Dec. 14, 1978	1831:13	105.8	35594.3	-47.5	39.9	-1.6	-75.9
82	59	Feb. 2, 1979	0729:07	28.6	66564.1	-19.7	28.5	-3.2	4.6
89	62	Feb. 4, 1979	1359:49	15.2	54486.8	-3.2	23.4	-3.1	8.2

See the text for an explanation of the terms used.

In Table 1 the following terms are used. The columns “date” and “orbit” indicate the date and the orbit at which a map, whose number is listed in the first column, was made. The third and following columns refer to the moment at which the center of the disk was scanned. The column “time” gives the time (UT) of this moment. The phase angle of the suborbiter point, which is the point on the planet right below the orbiter, is called the disk-centered phase angle, denoted by α_0 . Phase angles of other points on the disk may differ by 10° from this value for small values of α_0 and low altitudes. The distance between the orbiter and the planetary surface is given by the altitude in kilometers. The latitude and longitude of the suborbiter point are given by β_{orb} and λ_{orb} , respectively, whereas β_{sun} and λ_{sun} denote the latitude and longitude of the subsolar point, which is the point on the planet where the Sun is in the zenith direction. Latitudes and longitudes in the OCPP database are all measured in the celestial coordinate system with the x – y plane passing through the center of Venus and parallel to the ecliptic, with the Aries direction defining the positive x axis. Note that these are not the International Astronomical Union (IAU) Venus coordinates, and the system does not rotate with the Venus solid body rotation but is fixed in space.

Two operations were performed on I , P , and χ before they were compared to calculated results. First, we calculated for each pixel the relative Stokes parameter q (as defined below) from P and χ . The reason for this is that the method we use for our comparison, which is described in section 4, benefits from this transformation, as was shown by Knibbe et al. [1994]. Using Stokes parameters I , Q , and U , defined with respect to the local scattering plane [e.g., Chandrasekhar, 1950; Van de Hulst, 1957; Bohren and Huffman, 1983], we have

$$P = \frac{\sqrt{Q^2 + U^2}}{I}, \quad (1)$$

and

$$\tan(2\chi) = \frac{U}{Q}, \quad (2)$$

where χ is measured relative to the local scattering plane. Hence the relative Stokes parameter

$$q = Q/I = P \cos(2\chi), \quad (3)$$

where we adopt the convention that $\cos(2\chi)$ has the same sign as Q [Hovenier and Van der Mee, 1983]. According to, e.g., Chandrasekhar [1950],

$$q = \frac{I_l - I_r}{I_l + I_r}, \quad (4)$$

where I_l and I_r are the intensities parallel and perpendicular to the reference plane for the Stokes parameters, respectively. When $U = 0$, commonly $-q$ is used as a measure for the degree of linear polarization. We have not used U in our analysis, since molecules and spherical particles scatter light in such a way that, with our choice of the reference plane, U vanishes for single scattering and is close to zero in the case of multiple scattering. Therefore U contains little information on the optical properties of the atmospheric constituents.

Second, the values of q were resampled onto a regular grid of planetary longitude and latitude. The reason for this is as follows. All pixels at a certain wavelength correspond to a certain set of unevenly spaced locations on the planet. Due to the measurement procedure, these locations form slightly different, unevenly spaced, grids of latitude and longitude for different wavelengths. We used routines from Wessel and Smith [1991] to obtain values of q on a single evenly spaced grid over the planet. This enabled us to easily compare observations made at different wavelengths.

We conclude this section with some remarks concerning the accuracy of the values of q . Using the maximum error of P , which is 0.002 for 550 and 935 nm, taking partial derivatives of Eqs. (1)–(3) and assuming that the relative errors of I , Q , and U are equal, we estimate the maximum errors in q , as derived from P and χ , not to exceed $\Delta q_1 = 0.004$. We note that using an upper bound is appropriate for our method of analysis, although typical measurement errors may well be smaller. We estimate the errors in the values of q due to their resampling not to exceed $\Delta q_2 = 0.001$. Assuming that Δq_1 and Δq_2 are random and independent errors, we find that

$$\Delta q = \sqrt{\Delta q_1^2 + \Delta q_2^2} = 0.004 \quad (5)$$

is the maximum error in q .

3. Three Models of the Clouds of Venus to Investigate Particle Sizes

We have constructed three models of the clouds of Venus which are discussed in the present section. First, we discuss the properties of these models that remain fixed. Then, we discuss for each model the parameters that are varied. The polarization of Venus was calculated according to these models using a thoroughly tested adding/doubling code for exact multiple-scattering calculations [cf. De Haan *et al.*, 1987]. In section 5 the results are compared to the OCPP data, and the method used for this comparison is discussed in section 4.

The calculations were performed for 550 nm and 935 nm, since at these wavelengths the influences of absorbing and scattering molecules are smallest among the four wavelengths that were observed by the Pioneer Venus orbiter. This facilitates our investigations of particle sizes. We assumed the incident sunlight to be unpolarized at these wavelengths [e.g., Stenflo, 1994].

On describing our models, we use the same terminology as Kawabata *et al.* [1980], where the expression "cloud particles" refers to a size distribution similar to that described by Hansen and Hovenier [1974]. We employ the expression "haze particles" for particles that are smaller than the cloud particles deduced by Hansen and Hovenier [1974]. Figure 1 shows schematically our models. Models CM and HCM only have a mixed layer, whereas model H/CM also has a haze layer on top of a mixed layer. In model CM, the mixed layer consists only of cloud particles and molecules. In model HCM, the mixed layer consists of haze particles, cloud particles, and molecules. In model H/CM, the haze layer consists of haze particles (without molecules), and the

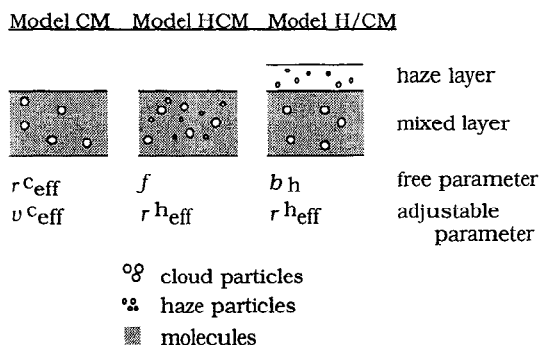


Figure 1. Schematic representation of the three models used for the cloud structure of Venus. Models CM and HCM only have a mixed layer, whereas model H/CM also has a haze layer on top of a mixed layer. In model CM the mixed layer consists only of cloud particles and molecules. In model HCM the mixed layer consists of haze particles, cloud particles, and molecules. In model H/CM the haze layer consists of haze particles, and the mixed layer consists of cloud particles and molecules. There is in each model a completely absorbing ground surface present.

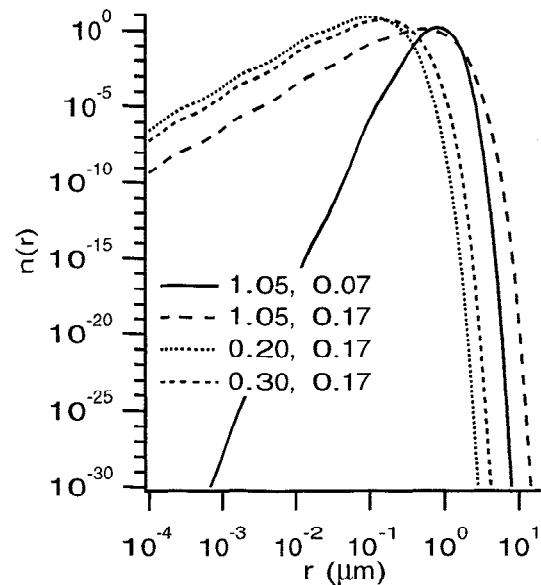


Figure 2. Gamma distributions, according to (6), displayed for different values of r_{eff} (in μm) and v_{eff} .

mixed layer consists of cloud particles and molecules. In each model a completely absorbing ground surface is present below the layer(s).

The wavelength dependent refractive index of the spherical cloud and haze particles in the three models corresponds to the concentrated sulfuric acid solution found by Hansen and Hovenier [1974], i.e., 1.44 and 1.43 at 550 and 935 nm, respectively. We assume that the single-scattering albedos for both cloud and haze particles equal unity. Single-scattering calculations for the spherical particles were performed using a Mie code [De Rooij and Van der Stap, 1984]. The optical thickness of the mixed layer of models CM, HCM, and H/CM is fixed at 30 for both wavelengths, in agreement with in situ measurements [Esposito *et al.*, 1983; Ragent *et al.*, 1985]. Our results are not very sensitive to this choice. For instance, for both wavelengths, values of q calculated for optical thicknesses of 25 and 35 differ generally less than 0.005 from values pertaining to an optical thickness of 30. For the optical thickness of molecular scattering in the mixed layer we adopt 0.25 at 550 nm and zero at 935 nm [cf. Hansen and Hovenier, 1974] for each model. The molecular depolarization factor is taken to be 0.079, after Alms *et al.* [1975] (see also De Haan [1987, chap. 2]).

Both cloud and haze particles are distributed in size according to a gamma distribution with effective radius r_{eff} and effective variance v_{eff} , respectively, as given by

$$n(r) = C r^{(1-3v_{\text{eff}})/v_{\text{eff}}} \exp[-r/(r_{\text{eff}} v_{\text{eff}})]. \quad (6)$$

Here $n(r)dr$ is the number of particles per unit volume with radius between r and $r + dr$, and C is a constant chosen such that $\int_0^\infty n(r)dr = 1$. Examples of this distribution are given in Figure 2. As shown by Hansen and Travis [1974], using a gamma distribution gives scattering properties that differ little from scat-

Table 2. Free Parameters and Adjustable Parameters for Models CM, HCM, and H/CM

Model	Free Parameter	Adjustable Parameter	Employed Values of Tune Parameter
CM	$0.1 \leq r_{\text{eff}}^c \leq 1.9$	v_{eff}^c	0.07, 0.17
HCM	$0.0 \leq f \leq 1.0$	r_{eff}^h	0.1, 0.2, 0.3, 0.4, 0.5
H/CM	$0.0 \leq b_h \leq 1.0$	r_{eff}^h	0.1, 0.2, 0.3, 0.4, 0.5

Effective radii are given in μm .

tering properties obtained using other size distributions having the same effective radius and effective variance. The bimodal distribution of model HCM consists of two unimodal distributions of haze and cloud particles, respectively.

Each model has one free parameter, which is varied between upper and lower bounds to obtain best agreement between calculated and observed values of q at 550 and 935 nm. The free parameters and their bounds are listed in Table 2 for each model. We introduced more freedom in our models by estimating the free parameters for various values of a different parameter. Such a parameter adjusts our model and is called an adjustable parameter. For each model the adjustable parameter is also listed in Table 2. The values listed in Table 2 were chosen such that values found in earlier research reported in the literature are bracketed. The parameters listed in Table 2 have the following meaning. The parameters r_{eff}^c and v_{eff}^c denote the effective particle radius and effective variance of the cloud particle size distribution, respectively. Similarly, the haze particle size distribution is specified by r_{eff}^h and v_{eff}^h . The parameter v_{eff}^h , which is not listed in Table 2, equalled 0.17 for all calculations reported in this paper.

The single-scattering properties of the cloud and haze particles in a volume element of the mixed layer of model HCM are described by the scattering matrix \mathbf{F} [cf. Van de Hulst, 1957; Bohren and Huffman, 1983], which is normalized so that the average of its one-one element over all directions equals unity. The free parameter f , where $0.0 \leq f \leq 1.0$, specifies the weight of the scattering matrix of the haze particles, \mathbf{F}_h , to the combined scattering matrix \mathbf{F} of cloud and haze particles, as follows:

$$\mathbf{F} = f \mathbf{F}_h + (1 - f) \mathbf{F}_c, \quad (7)$$

where \mathbf{F}_c denotes the scattering matrix of the cloud particles. An explicit expression for f in terms of particle number densities is given by

$$f = \left(1 + \frac{n^c G^c Q_{\text{sca}}^c(\lambda)}{n^h G^h Q_{\text{sca}}^h(\lambda)} \right)^{-1}. \quad (8)$$

Here n^c and n^h denote cloud and haze particle number densities, respectively; G^c and G^h denote average geometrical cross sections of cloud and haze particles, respectively; and $Q_{\text{sca}}^c(\lambda)$ and $Q_{\text{sca}}^h(\lambda)$ denote average

scattering efficiencies for cloud and haze particles, respectively, which depend on the wavelength λ . The physical meaning of f is that it specifies the relative scattering contribution of the haze particles to the total particulate scattering in the mixed layer. We have scaled f according to the wavelength dependent scattering coefficients. From hereon, all numerical values of f mentioned refer to a wavelength of 550 nm.

The haze optical thickness above the cloud layer is given by b_h and ranges between 0.0 and 1.0 for 550 nm. We have scaled b_h according to the wavelength dependent scattering efficiencies of haze particles to obtain values at 935 nm. A number of values for these efficiencies are given in Table 3, as well as a number of values of n^h/n^c for different f . From here on, all numerical values of b_h mentioned refer to a wavelength of 550 nm.

We compared theoretical values of Venus' spherical albedo according to models CM, HCM, and H/CM with the observationally determined values of 0.87 and 0.90 at wavelengths of 550 nm and 935 nm, respectively [cf. Travis, 1975; Moroz, 1983]. We found differences less than 0.01 between theoretical and observed values.

The choice of the free parameters and adjustable parameters was determined by the following considerations. Model CM is used to investigate whether the same cloud model as derived by Hansen and Hovenier [1974], for the same or different cloud particle sizes, can explain the selected polarization observations of the Pioneer Venus orbiter. This is done by using r_{eff}^c as a free parameter and keeping $v_{\text{eff}}^c = 0.07$. Further, by performing calculations also for $v_{\text{eff}}^c = 0.17$ it is investigated with model CM if the small particles that have been reported in the clouds of Venus could be part of a broader unimodal particle size distribution.

Model HCM is used to investigate whether the selected OCPP observations can be explained by a bimodal size distribution in the mixed layer, similar to the distribution reported by Knollenberg and Hunten [1980]. The relative scattering contribution of haze particles in the mixed layer is estimated, by using f as a free parameter. This is done for different haze effective particle radii, r_{eff}^h . Similarly, model H/CM is used to investigate whether we can find evidence for a thin haze layer, as reported by Kawabata et al. [1980]. The haze optical thickness is also estimated for various values of r_{eff}^h , since, as far as we know, there is no well-established value for this quantity. The model specification of mod-

Table 3. Properties of Cloud and Haze Particles at 550 and 935 nm

Cloud Particles					
$r_{\text{eff}}^c, \mu\text{m}$	v_{eff}^c	$G, \mu\text{m}^2$	Q_{sca}^{550}	Q_{sca}^{935}	
1.05	0.07	2.770	2.395	2.896	
1.05	0.17	1.897	2.478	2.908	
Haze Particles					
$r_{\text{eff}}^h, \mu\text{m}$	$G, \mu\text{m}^2$	Q_{sca}^{550}	Q_{sca}^{935}	n^h/n^c	n^h/n^c
				$f = 0.1$	$f = 0.5$
0.10	0.017	0.376	0.070	115.3	1037.9
0.20	0.069	1.728	0.552	6.2	55.6
0.30	0.155	2.773	1.344	1.7	15.4

Here G denotes the average geometrical cross section of the particles, Q_{sca}^{550} and Q_{sca}^{935} denote the scattering efficiencies at 550 and 935 nm, respectively. Also shown are ratios of haze and cloud particle number densities, denoted by n^h/n^c , calculated for $f = 0.1$ and 0.5 at 550 nm, where $v_{\text{eff}}^c = 0.07$.

els HCM and H/CM is completed by giving the cloud particle size distribution for these models. We used the same distribution as deduced by *Hansen and Hovenier* [1974], i.e., $r_{\text{eff}}^c = 1.05 \mu\text{m}$, and $v_{\text{eff}}^c = 0.07$. Different results would be obtained when using a different cloud particle size distribution. Our choice, however, namely, the cloud model of *Hansen and Hovenier* [1974], provides us with a common reference for our three models.

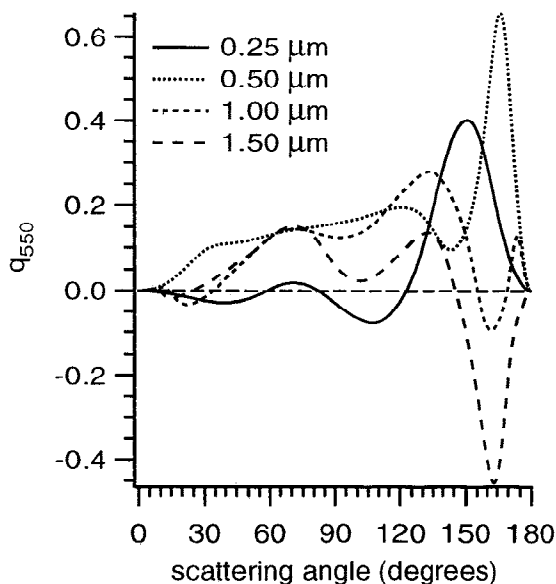


Figure 3. Theoretical values of q_{550} as functions of scattering angle of singly scattered light by an ensemble of spheres for different values of r_{eff} . The refractive index of the spheres corresponds to a concentrated sulfuric acid solution, i.e., it equals 1.44 at 550 nm. The results pertain to unpolarized incident light, and $v_{\text{eff}} = 0.07$.

That is, in model CM, r_{eff}^c and v_{eff}^c are changed with respect to the values of *Hansen and Hovenier* [1974], and in models HCM and H/CM the scattering contribution of small particles is varied.

In order to select the most informative maps regarding haze particles, we now consider single-scattering properties of haze and cloud particles, and how they vary with r_{eff} and v_{eff} . These are relevant, since the shape of the polarization as a function of scattering angle of light reflected by clouds is mainly determined by single scattering in the upper part of the clouds. Results of calculations taking all orders of scattering into account will be presented in sections 4 and 5. Figures 3 – 6 show the influence of r_{eff} and v_{eff} on q at 550 and 935 nm, denoted by q_{550} and q_{935} , respectively, for singly scattered light, where the incident light is unpolarized. In Figures 3 and 4, we see that between scattering angles of 150° and 170° , q is very sensitive to changes in r_{eff} . For this reason, we analyzed two OCPP maps made at phase angles between 10° and 30° , as described in the following sections, since the phase angle equals 180° minus the scattering angle. However, Figure 4 also shows that at scattering angles near 90° q_{935} is very different for $r_{\text{eff}} = 0.25 \mu\text{m}$ than for the other values of r_{eff} . For this reason, we analyzed two OCPP maps having phase angles near 90° as well.

Figures 5 and 6 show the sensitivity of the linear polarization of singly scattered light to v_{eff} . Apparently, for most scattering angles the narrowest size distribution leads to the highest absolute values of q , but not between approximately 30° and 105° at 550 nm, and near a scattering angle of 150° at 935 nm. Further, at both wavelengths the influence of v_{eff} appears to be smaller at scattering angles near 90° than between about 150° and 170° .

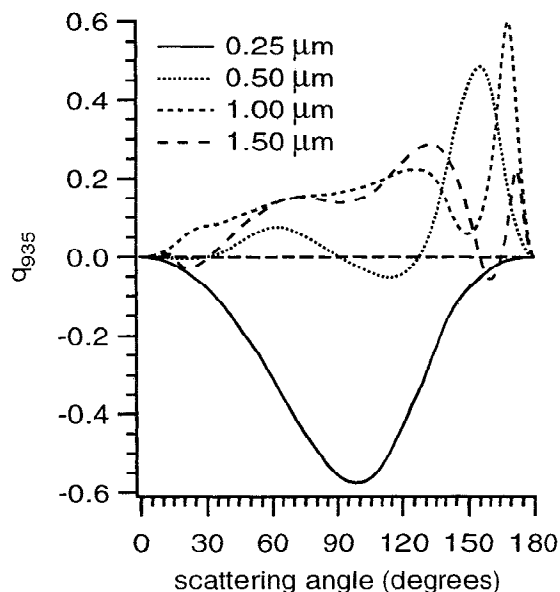


Figure 4. Same as Figure 3, but for q_{935} and a refractive index of 1.43.

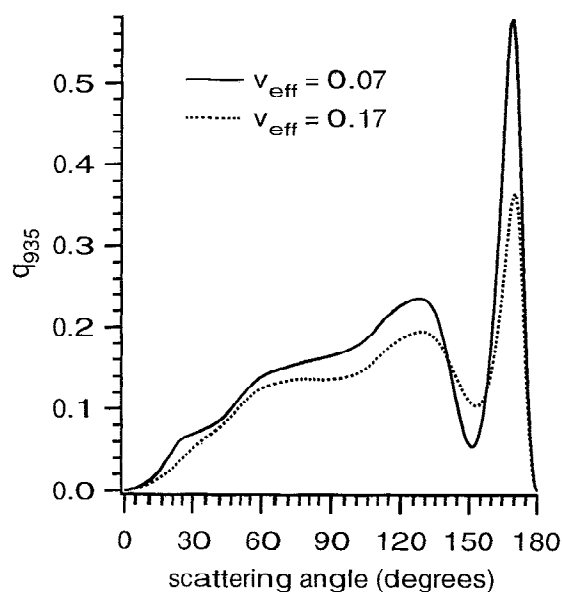


Figure 6. Same as Figure 5, but for q_{935} and a refractive index of 1.43.

4. Feature Space and Method of Analysis

In this section, we explain a new method using feature space for analyzing the OCPP data. This method uses the results of multiple-scattering calculations applied to the cloud models presented in section 3.

The method is aimed at a pixel-wise analysis, in contrast to the analysis of values averaged over regions containing many pixels, as presented by Kawabata *et al.* [1980]. Our method takes advantage of the high spatial resolution of the OCPP data. For this purpose, we extended the concept of a feature space, as presented by, e.g., Mehl [1994], to polarized light. In our method, we use a two-dimensional feature space. In principle, it can

be extended to more dimensions. Each pixel of a resampled OCPP map corresponds to a point in this feature space. The x coordinate and y coordinate of such a point are given by q at 550 nm and 935 nm, respectively, indicated by q_{550} and q_{935} . Similarly, theoretical values of q_{550} and q_{935} also correspond to points in the feature space. As an example, Figure 7 shows observed values of q_{550} and q_{935} displayed in the feature space. Significant variations of q_{550} and q_{935} occur, caused partly by differences in scattering geometry and composition of the atmosphere.

The advantage of using this feature space is that it enables severe tests of our models for the clouds of Venus

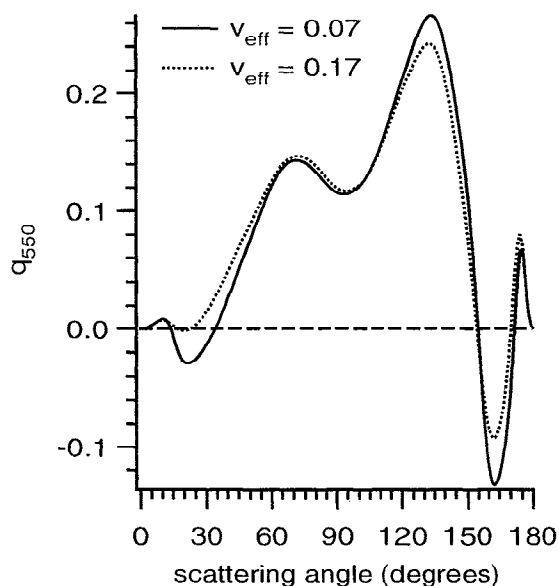


Figure 5. Same as Figure 3, but for different values of v_{eff} . Here $r_{\text{eff}} = 1.05 \mu\text{m}$.

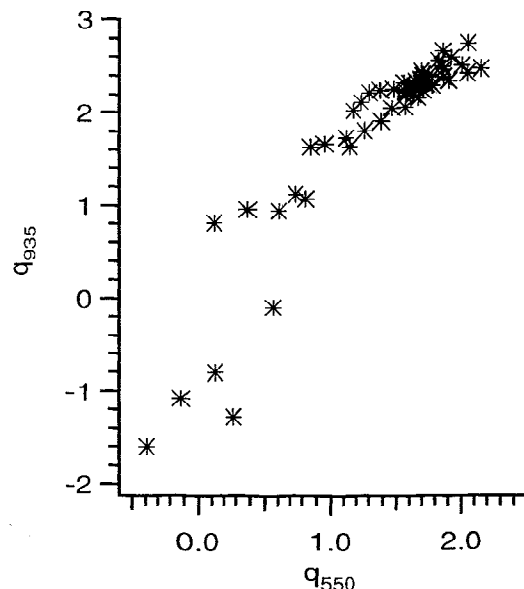


Figure 7. Observed values of q_{550} and q_{935} in percent taken from map 16 from the band which extends from 15° north to 15° south of the equator.

on a pixel-wise basis, by separating the variations due to differences in scattering geometry from those due to composition differences. Testing can simply be done by demanding that the distance in the feature space between the points corresponding to observed and theoretical values of q is less than some specific bound, L . The uncertainties in the locations of the calculated points are negligible compared to those of the observed points. Therefore, in order to determine L , we used the maximum errors of the observed values of q_{550} and q_{935} , Δq_{550} and Δq_{935} , respectively. Assuming that the errors of q at the two wavelengths, as determined in section 2, are random and independent, it follows that

$$L = \sqrt{\Delta q_{550}^2 + \Delta q_{935}^2} = 0.006. \quad (9)$$

The following example serves to show how the feature space is used in our method. Figure 8 shows calculated and observed values of q pertaining to the suborbiter point of map 89 displayed in the feature space. In this figure, the asterisk denotes observed values of q , and the big circle around it, which has a radius L , corresponds to the error in the measurements. The curves labeled 0.07 and 0.17 connect calculated values of q according to model CM for $v_{\text{eff}}^c = 0.07$ and 0.17, respectively, for different values of r_{eff}^c . These values of r_{eff}^c range from 0.1 μm to 1.9 μm in steps of 0.1 μm .

In order to determine whether model CM is valid for this pixel, we proceed as follows. We determine an es-

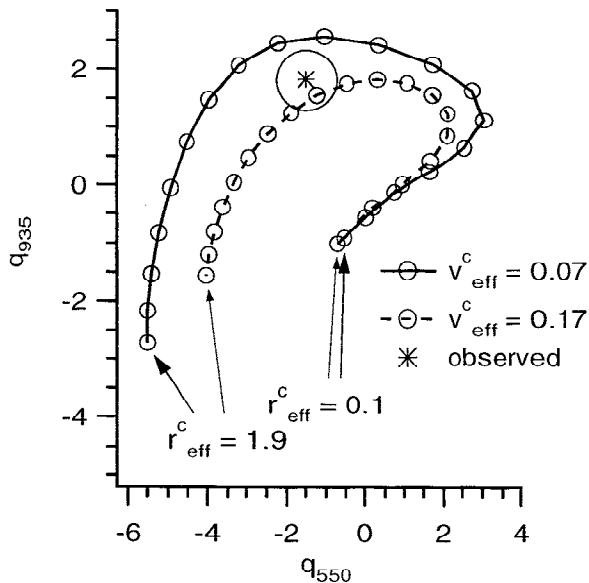


Figure 8. Theoretical values of q_{550} and q_{935} , both in percent, calculated for the suborbiter point of map 89 taking all orders of scattering into account, displayed in the feature space. The small circles pertain to calculations for model CM, for different values of r_{eff}^c increasing from 0.1 μm to 1.9 μm in steps of 0.1 μm . The solid and dashed curves connect calculations for $v_{\text{eff}}^c = 0.07$ and 0.17, respectively. The asterisk denotes the observed values, and the big circle around it corresponds to the maximal measurement error.

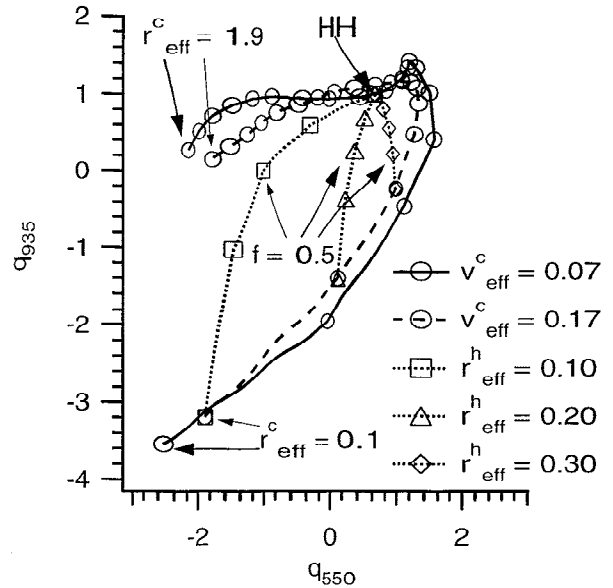


Figure 9. Theoretical values of q_{550} and q_{935} in percent for the suborbiter point of map 82. The circles pertain to calculations for model CM, for different values of r_{eff}^c increasing from 0.1 μm to 1.9 μm in steps of 0.1 μm . Squares, triangles, and diamonds pertain to model HCM if $r_{\text{eff}}^h = 0.1 \mu\text{m}$, 0.2 μm , and 0.3 μm , respectively. Here f is varied from 0.0 to 1.0 in steps of 0.25. The point on the solid line indicated by the arrow labeled HH indicates q_{550} and q_{935} calculated according to the model of Hansen and Hovenier [1974]. Results for model HCM if $f = 1.0$ coincide with results for model CM if $r_{\text{eff}}^c = r_{\text{eff}}^h$ and $v_{\text{eff}}^c = 0.17$.

timate of r_{eff}^c for $v_{\text{eff}}^c = 0.07$ using a method similar to inverse parabolic interpolation [see Press *et al.*, 1992, chap. 10]. This estimate corresponds to the point on the curve pertaining to $v_{\text{eff}}^c = 0.07$, which is closest to the asterisk. It is clear from Figure 8 that the distance between the calculated values of q for this estimate and the observed values is larger than L . Therefore model CM is not valid for this pixel for $v_{\text{eff}}^c = 0.07$. Next we determine the distance between observed and calculated values of q pertaining to the estimate of r_{eff}^c for $v_{\text{eff}}^c = 0.17$. Model CM with the chosen values for v_{eff}^c would not be valid for this pixel if this distance would also be larger than L . It appears, however, from Figure 8 that model CM is valid for this pixel for $v_{\text{eff}}^c = 0.17$, with an estimated r_{eff}^c of approximately 1.1 μm .

Generalizing the discussion of our example, we treat each model as follows. We determine estimates of its free parameter, using a method similar to parabolic interpolation [Press *et al.*, 1992, chap. 10], for each value of the corresponding adjustable parameter. Then we check if the calculated values of q for these estimates are close enough to the observed values. Here, "close enough" means having a distance in the feature space to the observed point which is smaller than or equal to L . A model is called valid only if this happens for at least one value of the chosen adjustable parameters. In principle, more than a single model can be valid.

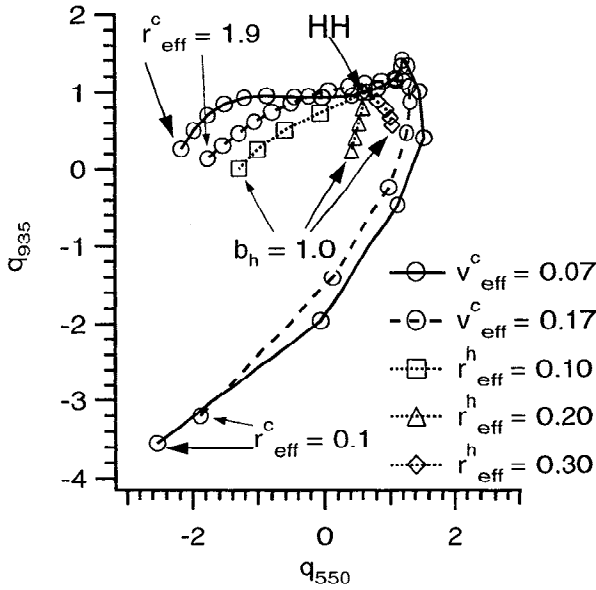


Figure 10. Same as Figure 9, but for model H/CM instead of model HCM, and for different values of b_h increasing from 0.0 to 1.0 in steps of 0.25.

We will now show theoretical results for the suborbiter point of map 82 in Figures 9 and 10. The circles in both figures pertain to calculations for model CM. The solid and dashed curves connect results for different values of r_{eff}^c , increasing from $0.1 \mu\text{m}$ to $1.9 \mu\text{m}$ in steps of $0.1 \mu\text{m}$, for $v_{\text{eff}}^c = 0.07$ and 0.17 , respectively. The other symbols in Figures 9 and 10 pertain to calculations for models HCM and H/CM, respectively. We mention that it is not necessary to discuss the results for models HCM and H/CM, for $r_{\text{eff}}^h = 0.4 \mu\text{m}$ and $0.5 \mu\text{m}$, since these would virtually coincide with q_{550} and q_{935} calculated using model CM.

The points on the solid curves in Figures 9 and 10 indicated by the arrows labeled HH pertain to the results for the reference model of Hansen and Hovenier [1974]. These figures serve to show that increasing the scattering contribution of haze particles within the mixed layer, as in model HCM, or of increasing the haze optical thickness, as in model H/CM, have nearly the same effects on q . For other phase angles we found the same result.

The polarization of the reflected light is most sensitive to the composition of the top of the atmosphere. This is illustrated by the results shown in Figures 9 and 10. For instance, for $r_{\text{eff}}^h = 0.2 \mu\text{m}$, we see that the polarization in Figure 9 is about the same for $f = 0.25$ to that in Figure 10 for $b_h = 0.5$. This means that an optical thickness of haze particles within the mixed layer of $0.25 \times 30 = 7.5$ has about the same effect as a haze layer with $b_h = 0.5$ in model H/CM. So, in this case, 15 times more haze particles per unit area are needed within the mixed layer cloud HCM model than above it in the haze layer of model H/CM.

Results for a phase angle of 97.1° are presented in Figure 11. This figure shows results of theoretical cal-

culations taking all orders of scattering into account for a point 30° west of the suborbiter point of map 16. These results are typical for other points of map 16 and also of map 21. The asterisk in Figure 11 denotes the observed values and the solid and dashed curves connect calculated results according to model CM for $v_{\text{eff}}^c = 0.07$ and 0.17 , respectively. Results for $1.0 \mu\text{m} < r_{\text{eff}}^c \leq 1.9 \mu\text{m}$ are not displayed, since these are too close to the results for $r_{\text{eff}}^c = 1.0 \mu\text{m}$ to be clearly distinguished in Figure 11. The dotted curve connects results according to model H/CM if $r_{\text{eff}}^h = 0.2 \mu\text{m}$. This figure shows that good agreement with the observed values is obtained for model H/CM with $r_{\text{eff}}^h = 0.2 \mu\text{m}$ and, say, $b_h = 0.12$. A similar good agreement can be obtained when model HCM is used instead of model H/CM. The differences between the theoretical results of Figures 8, 10, and 11 are mainly caused by differences in phase angle.

5. Analysis of Observed Polarization

In this section, we present results of our analysis of the polarization of Venus as observed by the Pioneer Venus orbiter using theoretical calculations. We used the feature space, as described in the previous section, to analyze maps 16, 21, 82, and 89 from the OCPP database which is described in section 2, using the models which are described in section 3.

We present results for pixels which were resampled with a resolution of 10° in latitude and longitude. These results are representative for those obtained with different resolutions. We discuss the four analyzed maps in

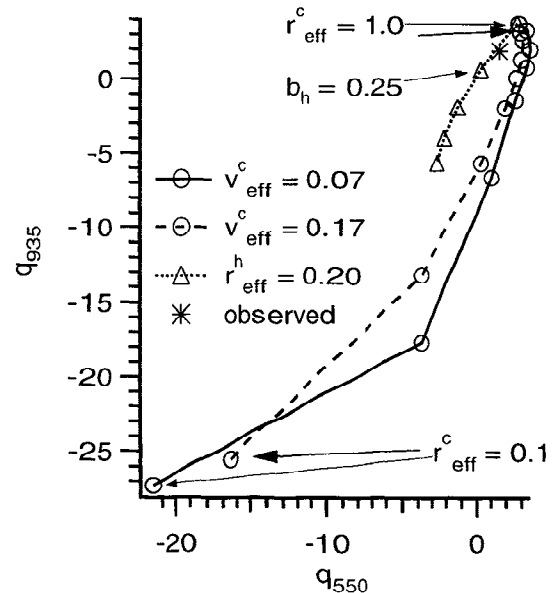


Figure 11. Same as Figure 8, but for a point 30° west of the suborbiter point of map 16. Here the circles pertain to model CM with different values of r_{eff}^c increasing from $0.1 \mu\text{m}$ to $0.6 \mu\text{m}$ in steps of $0.1 \mu\text{m}$, and from $0.6 \mu\text{m}$ to $1.0 \mu\text{m}$ in steps of $0.2 \mu\text{m}$. The triangles on the dotted curve pertain to model H/CM if $r_{\text{eff}}^h = 0.2 \mu\text{m}$ for b_h increasing from 0.0 to 1.0 in steps of 0.25. The asterisk denotes the observed values for this point.

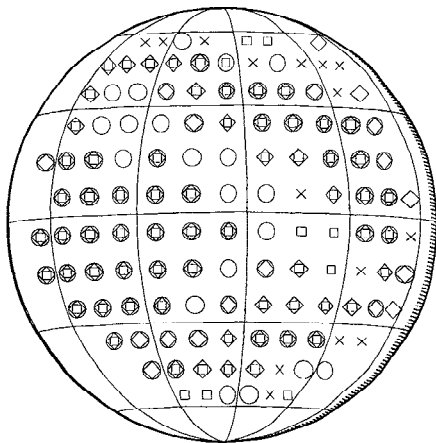


Figure 12. Locations of pixels for which our models are valid, for map 89, displayed on a projected grid of latitude and longitude, with a grid spacing of 30° in both directions. The suborbiter point is located at the center of the disk. Circles correspond to model CM, diamonds to model HCM, and squares to model H/CM. Crosses indicate locations of resampled pixels where no model was valid. The area on the right which is densely packed with dots corresponds to the visible part of the nightside of Venus.

the order of increasing disk-centered phase angle, i.e., 15.2° , 28.6° , 97.1° , and 105.8° for maps 89, 82, 16, and 21, respectively. Starting with map 89, we first consider the locations of the pixels for which models CM, HCM, and H/CM are valid for the values of the adjustable parameters listed in Table 2. For each model, these pixels form regions that cover large parts of the observed area. Figure 12 shows these locations for model CM (displayed

by circles), model HCM (diamonds), and for model H/CM (squares). Other locations for which resampled observations are available are indicated by crosses. In this figure, we see that at a large number of locations all three models are valid. Theoretical curves in the feature space, which are not shown here, indicate that the size of the part of the observed area for which the three models are valid would even increase when using a finer spaced grid of the values of the adjustable parameters. We conclude that the locations of the pixels of map 89 where the models are valid for the values of the adjustable parameters listed in Table 2 do not allow a preference for one of these models.

Next we consider the estimates of the free parameters for the different models from the comparison with map 89. Although we cannot determine a preference for one model, the estimates for our models give relevant information about the particle sizes in the clouds of Venus. For instance, in Figure 13 we see the estimates of r_{eff}^c as a function of latitude for $v_{\text{eff}}^c = 0.07$ and 0.17 , which were determined using model CM. These local values of r_{eff}^c , which vary between $0.95 \mu\text{m}$ and $1.10 \mu\text{m}$ if $v_{\text{eff}}^c = 0.07$, are consistent with the globally averaged value of $1.05 \mu\text{m}$ deduced by Hansen and Hovenier [1974]. Estimates of r_{eff}^c vary between 0.85 and $1.15 \mu\text{m}$ if $v_{\text{eff}}^c = 0.17$ and are generally smallest at high latitudes, where no estimates were valid for $v_{\text{eff}}^c = 0.07$.

The estimated scattering contribution of haze particles for model HCM corresponds to values of f sometimes as large as 0.9 . The highest values are found at high latitudes and near the terminator. Estimates in the equatorial region are generally of the order of 0.2 .

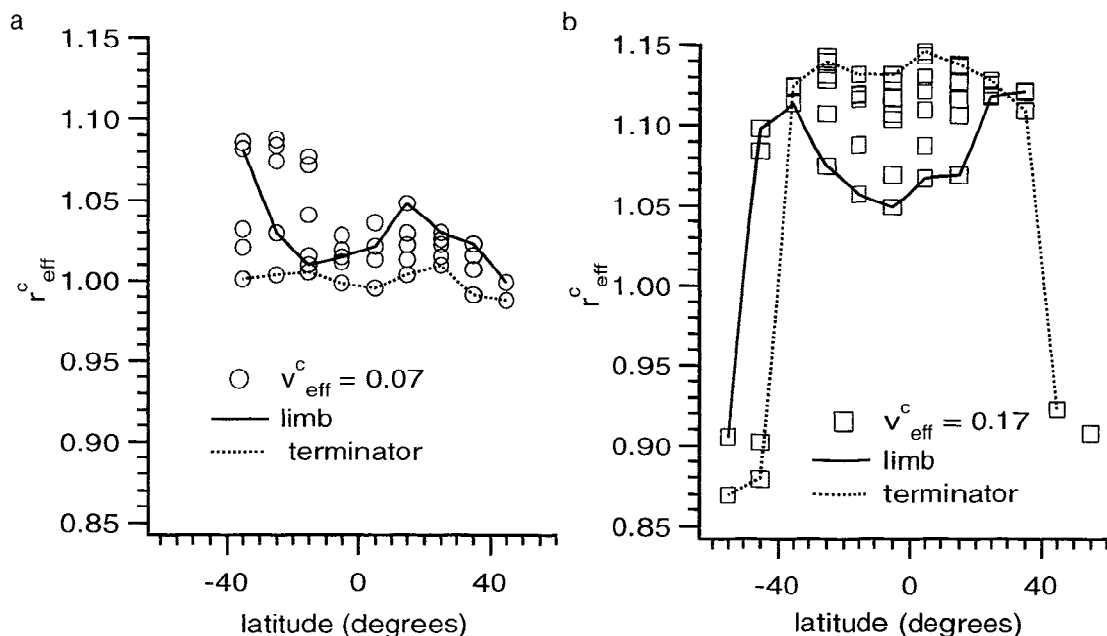


Figure 13. Estimates of r_{eff}^c for map 89 as a function of latitude, for $v_{\text{eff}}^c = 0.07$ (a, circles) and 0.17 (b, squares). Different estimates at the same latitude correspond to different longitudes. The solid and dotted curves connect the estimates closest to the planetary limb and morning terminator, respectively.

For model H/CM, we find maximal values of b_h of the order of 0.8, where the highest values are found near the poles. Near the equator, estimates of b_h are of the order of 0.1.

The analysis of map 82 leads to similar results as that of map 89, except for the pixels for which model CM is valid. These cover practically the entire observed area of this map, whereas those for map 89 covered only the largest part of the observed area. This difference is caused by the weaker dependence of q_{550} and q_{935} on v_{eff}^c at the phase angles of map 82 than at those of map 89, as can be seen in Figures 9 and 8, which can be compared to the single-scattering results shown in Figures 5 and 6. So for map 82, we do not need a finer grid of values of v_{eff}^c to cover the observed area with pixels for which model CM is valid.

Summarizing the results of our analysis of maps 82 and 89 concerning the presence of haze particles in the upper region of the clouds of Venus, we found the following. The observed values of q of these maps at 550 and 935 nm are for large parts of the planet explicable without haze particles. Already, *Kawabata et al.* [1980] showed that at phase angles between 10° and 30° the disk-averaged values of the polarization obtained from Pioneer Venus observations are similar to earthbound observations at these wavelengths, which were interpreted by *Hansen and Hovenier* [1974] without invoking haze particles. However, our investigations using models HCM and H/CM have shown that the polarization of these maps is also in agreement with the presence of haze particles. That is, the possibility of haze particles, which may be present within or above a mixed layer, is not ruled out by Pioneer Venus observations such as those of maps 82 and 89. The estimates of b_h that we find in the polar regions are similar to those reported by *Kawabata et al.* [1980], but our equatorial values are larger.

The situation is different for maps 16 and 21. For these maps we found, namely, no pixels for which model

CM is valid for the chosen values of the adjustable parameters. Even employing values of v_{eff}^c in between the values listed in Table 2 would not increase the number of such pixels. That is, clearly, model CM fails the test at phase angles near 90° for the parameter values that we used, contrary to the tests at phase angles between 10° and 30° . On the other hand, the observed areas of maps 16 and 21 are largely covered by pixels for which models HCM and H/CM are valid. We did not find such pixels for these models if $r_{\text{eff}}^h = 0.1 \mu\text{m}$. As shown in Figure 14 for map 16, the number of these pixels for model HCM is about the same as that for model H/CM. The same holds for map 21. In addition, theoretical curves in the feature space as compared to observations indicate that a larger part of the observed area would be covered by such pixels when using a finer spaced grid of the values of r_{eff}^h , by adding values in between $0.15 \mu\text{m}$ and $0.35 \mu\text{m}$.

The retrieved haze characteristics from maps 16 and 21 are similar to those deduced from maps 82 and 89. However, because maps 16 and 21 can only be explained with our models that include haze particles, we consider the values derived from maps 16 and 21 as more significant than the values derived from maps 82 and 89. The estimates of f lie between 0.1 and 0.5 for map 16 and between 0.1 and 0.7 for map 21. The estimates of b_h lie between 0.1 and 0.3 for map 16 and between 0.1 and 0.6 for map 21. The highest values are sometimes but not always found at high latitudes. Estimates of f in the equatorial regions are of the order of 0.2, as well as those of b_h . Examples of these results are shown in Figure 15 and 16 for map 16. For this map, near the terminator, no unambiguous increase of haze is found.

Summarizing the results of our analysis of maps 16 and 21, we find convincing evidence that only models having haze particles in the upper region of the clouds of Venus can explain the observed polarization.

6. Conclusions

We showed that combining two-wavelength polarimetry at a suitable phase angle is very informative of atmospheric properties, as opposed to conventional focus on the angular dependence of the polarization. This permits an automated pixel-wise interpretation, for which no assumptions need to be made about the horizontal homogeneity of the atmosphere, which on the contrary, would be needed to investigate the angular dependence of the polarization. Using this approach, we were able to interpret the spatial dependence of the polarization over the entire disk of Venus in terms of variation of cloud and haze properties.

The cloud and haze properties were derived using three different models for the atmosphere of Venus. The first model, in which only the cloud particle size distribution was adjusted to match the observations, was found unable to explain observations at all phase angles analyzed. The two other models, in which only proper-

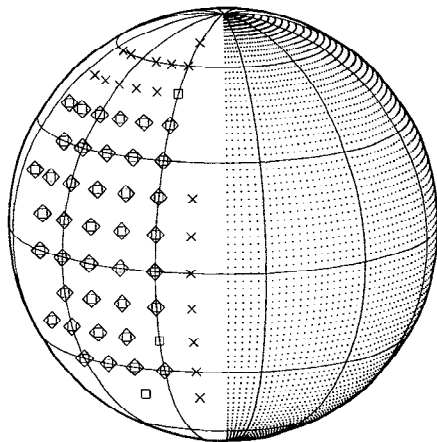


Figure 14. Same as Figure 12, but for map 16. Diamonds correspond to model HCM, and squares to model H/CM.

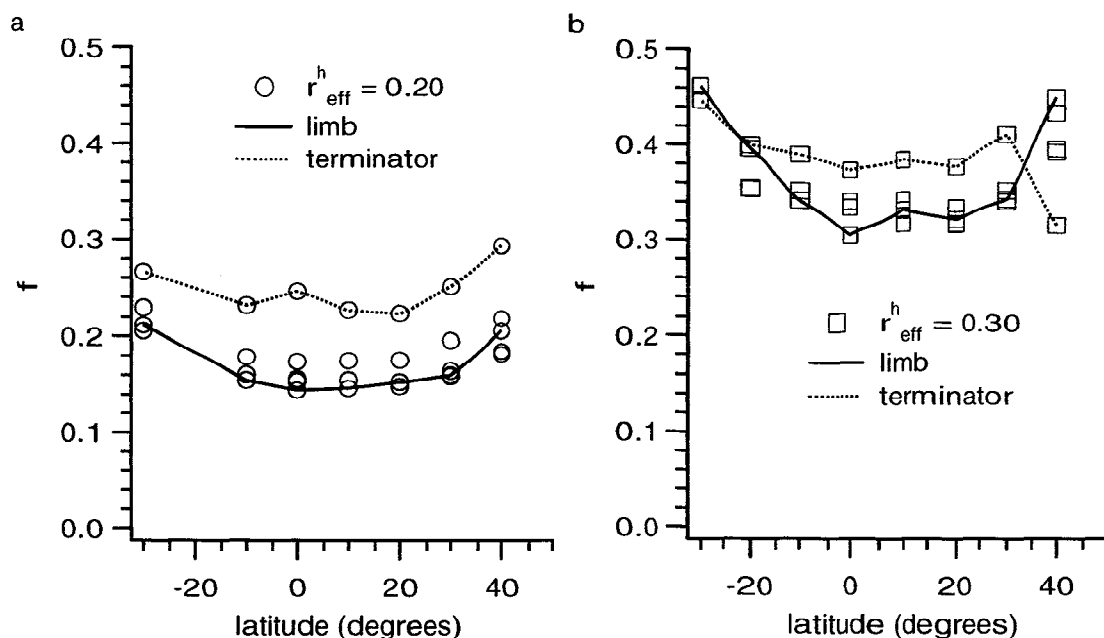


Figure 15. Estimates of f for map 16 as a function of latitude, for $r_{\text{eff}}^h = 0.2$ μm (a, circles), and 0.3 μm (b, squares). Different circles or squares at the same latitude correspond to different longitudes. The solid and dotted curves connect the estimates closest to the planetary limb and morning terminator, respectively.

ties of haze particles, either within or above the cloud layer, were adjusted, could explain a large portion of the observations at all phase angles analyzed. It therefore follows from our analysis that best results are obtained with a fixed cloud particle size distribution and haze properties that vary over the planet.

We derived cloud effective particle radii between 0.85 μm and 1.15 μm , where the smallest values were found at high latitudes. Effective radii of the haze particles of 0.2 μm or 0.3 μm were deduced. Considering haze

particles mixed with cloud particles in a single layer, we derived a contribution of the haze particles to the total atmospheric scattering coefficient at 550 nm of up to 70% at high latitudes, but of the order of 20% for the equatorial region. Considering haze particles situated above a layer with cloud particles, we deduced values of the haze optical thickness at 550 nm of up to 0.6, occurring mostly at high latitudes, whereas generally values of the order of 0.1 were found in the equatorial region.

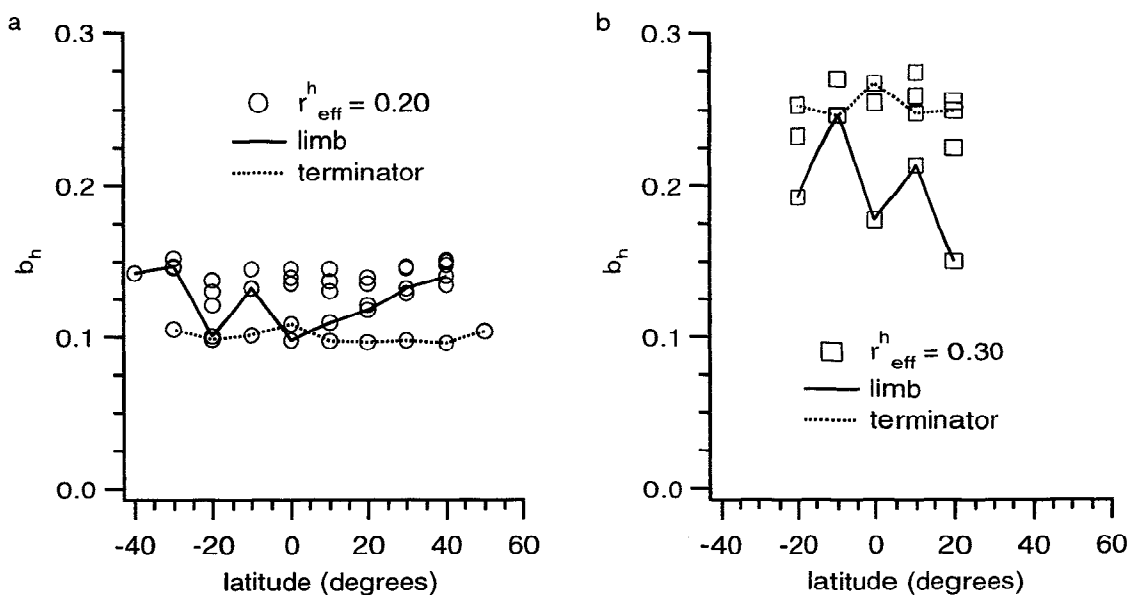


Figure 16. Same as Figure 15, but for b_h in lieu of f .

The approach presented in this work may in principle be extended to more wavelengths and seems promising for automated analysis of satellite polarization data, such as are being obtained by the photopolarimeter/radiometer (PPR) experiment [Russell et al., 1992], which flies on the Galileo mission, and by the experiment polarization and directionality of the Earth's reflectances (POLDER) [Deschamps et al., 1994], which flies on the ADEOS mission, and will be obtained by the Earth observing scanning polarimeter (EOSP) [Travis, 1992], which is scheduled for the EOS mission.

Acknowledgments. We gratefully acknowledge the detailed comments of two anonymous reviewers. We further acknowledge stimulating discussions with M. I. Mishchenko about an earlier version of this paper. This work has been supported in part by a Columbia University research program funded by NASA Goddard Institute for Space Studies.

References

- Alms, G. R., A. K. Burnham, and W. H. Flygare, Measurements of the dispersion in the polarizability tensor, *J. Chem. Phys.*, **63**, 3321–3326, 1975.
- Bohren, C. F., and D. R. Huffman, *Absorption and Scattering of Light by Small Particles*, John Wiley, New York, 1983.
- Chandrasekhar, S., *Radiative Transfer*, Oxford Univ. Press, New York, 1950.
- Colin, L., The Pioneer Venus program, *J. Geophys. Res.*, **85**, 7575–7598, 1980.
- Colin, L., and D. M. Hunten, Pioneer Venus experiment descriptions, *Space Sci. Rev.*, **20**, 451–525, 1977.
- De Haan, J. F., Effects of aerosols on the brightness and polarization of cloudless planetary atmospheres, Ph.D. Thesis, Free Univ., Amsterdam, The Netherlands, 1987.
- De Haan, J. F., P. B. Bosma, and J. W. Hovenier, The adding method for multiple scattering calculations of polarized light, *Astron. Astrophys.*, **183**, 371–391, 1987.
- De Rooij, W. A., and C. C. A. H. van der Stap, Expansion of Mie scattering matrices in generalized spherical functions, *Astron. Astrophys.*, **131**, 237–248, 1984.
- Deschamps, P.-Y., F.-M. Bréon, M. Leroy, A. Podaire, A. Bricaud, J.-C. Buriez, and G. Sèze, The Polder mission: Instrument characteristics and scientific objectives, *IEEE Trans. Geosci. Remote Sens.*, **32**, 598–615, 1994.
- Esposito, L. W., R. G. Knollenberg, M. Y. Marov, O. B. Toon, and R. B. Turco, The clouds and hazes of Venus, in *Venus*, edited by D. M. Hunten, L. Colin, T. M. Donahue, and V. I. Moroz, pp. 484–564, Univ. of Ariz. Press, Tucson, 1983.
- Grinspoon, D. H., J. B. Pollack, B. R. Sitton, R. W. Carlson, L. W. Kamp, K. H. Baines, T. Encrenaz, and F. W. Taylor, Probing Venus's cloud structure with Galileo NIMS, *Planet. Space Sci.*, **41**, 515–542, 1993.
- Hansen, J. E., and J. W. Hovenier, Interpretation of the polarization of Venus, *J. Atmos. Sci.*, **31**, 1137–1160, 1974.
- Hansen, J. E., and L. D. Travis, Light scattering in planetary atmospheres, *Space Sci. Rev.*, **16**, 527–610, 1974.
- Hovenier, J. W., and C. V. M. Van der Mee, Fundamental relationships relevant to the transfer of polarized light in a scattering atmosphere, *Astron. Astrophys.*, **128**, 1–16, 1983.
- Kawabata, K., D. L. Coffeen, J. E. Hansen, W. A. Lane, Makoto Sato, and L. D. Travis, Cloud and haze properties from Pioneer Venus polarimetry, *J. Geophys. Res.*, **85**, 8129–8140, 1980.
- Knibbe, W. J. J., J. F. De Haan, J. W. Hovenier, and L. D. Travis, Spatial variations of Venus' cloud properties derived from polarimetry, in *Atmospheric Sensing and Modeling*, edited by R. Santer, *Proc. Int. Soc. Opt. Eng.*, **2311**, 47–57, 1994.
- Knollenberg, R. G., and D. M. Hunten, The microphysics of the clouds of Venus: Results of the Pioneer Venus particle size spectrometer experiment, *J. Geophys. Res.*, **85**, 8039–8058, 1980.
- Krasnopolsky, V. A., Venus spectroscopy in the 3000–8000 Å region by Venera 9 and 10, in *Venus*, edited by D. M. Hunten, L. Colin, T. M. Donahue, and V. I. Moroz, pp. 459–483, Univ. of Ariz. Press, Tucson, 1983.
- Marov, M. Y., V. E. Lystsev, V. N. Lebedev, N. L. Lukashevich, and V. P. Shari, The structure and microphysical properties of the Venus clouds: Venera 9, 10, 11 data, *Icarus*, **44**, 608–639, 1980.
- Mehl, W., Data analysis – Processing requirements and available software tools, in *Imaging Spectroscopy – A Tool for Environmental Observations*, edited by J. Hill and J. Megier, pp. 89–107, Kluwer Acad., Norwell, Mass., 1994.
- Moroz, V. I., Stellar magnitude and albedo data of Venus, in *Venus*, edited by D. M. Hunten, L. Colin, T. M. Donahue, and V. I. Moroz, pp. 27–35, Univ. of Ariz. Press, Tucson, 1983.
- Press, W. H., S. A. Teukolsky, W. T. Vetterling, and B. P. Flannery, *Numerical Recipes*, Cambridge Univ. Press, New York, 1992.
- Ragent, B., and J. Blamont, The structure of the clouds of Venus: Results of the Pioneer Venus nephelometer experiment, *J. Geophys. Res.*, **85**, 8089–8105, 1980.
- Ragent, B., L. W. Esposito, M. G. Tomasko, M. Y. Marov, V. P. Shari, and V. N. Lebedev, Particulate matter in the Venus atmosphere, *Adv. Space Res.*, **5**, 85–115, 1985.
- Russell, E., L. Watts, S. Pellicori, and D. Coffeen, Orbiter cloud photopolarimeter for the Pioneer Venus mission, *Proc. Soc. Photo. Opt. Instrum. Eng.*, **112**, 28–44, 1977.
- Russell, E. E., F. G. Brown, R. A. Chandos, W. C. Fincher, L. F. Kubel, A. A. Lacis, and L. D. Travis, Galileo photopolarimeter/radiometer experiment, *Space Sci. Rev.*, **60**, 531–563, 1992.
- Sato, M., L. D. Travis, and K. Kawabata, Photopolarimetry analysis of the Venus atmosphere in polar regions, *Icarus*, **124**, 569–585, 1996.
- Stenflo, J. O., *Solar Magnetic Fields*, Kluwer Acad., Norwell, Mass., 1994.
- Travis, L. D., On the origin of ultraviolet contrasts on Venus, *J. Atmos. Sci.*, **32**, 1190–1200, 1975.
- Travis, L. D., Imaging and polarimetry with the Pioneer Venus orbiter cloud photopolarimeter, *Proc. Soc. Photo. Opt. Instrum. Eng.*, **112**, 28–44, 1979.
- Travis, L. D., Earth observing scanning polarimeter, in *Long Term Monitoring of Global Climate Forcings and Feedbacks*, edited by J. Hansen, W. Rossow, and I. Fung, *NASA Conf. Publ.*, **3234**, 40–46, 1992.
- Van de Hulst, H. C., *Light Scattering by Small Particles*, John Wiley, 1957. (Also Dover, New York, 1981.)
- Wessel, P., and W. H. F. Smith, Free software helps map and display data, *Eos Trans. AGU*, **72**, 441–446, 1991.
- J. F. de Haan, J. W. Hovenier, and W. J. J. Knibbe, Department of Physics and Astronomy, Free University, De Boelelaan 1081, NL-1081 HV Amsterdam, The Netherlands. (e-mail: johan@nat.vu.nl; hovenier@nat.vu.nl; willemj@nat.vu.nl)
- L. D. Travis, NASA Goddard Institute for Space Studies, 2880 Broadway, New York, NY 10025. (e-mail: pldt@giiss.nasa.gov)

(Received August 7, 1996; revised January 17, 1997; accepted January 30, 1997.)